ROUGHNESS-RESOLVED LES OF ADDITIVE MANUFACTURING-LIKE CHANNEL FLOWS

Serge Meynet, Alexis Barge, Vincent Moureau, Guillaume Balarac, Ghislain Lartigue, Abdellah Hadjadj

ROUGHNESS-RESOLVED LES OF ADDITIVE MANUFACTURING-LIKE CHANNEL FLOWS

Serge Meynet[1], Alexis Barge[2], Vincent Moureau[1], Guillaume Balarac[2,3], Ghislain Lartigue[1], Abdellah Hadjadj[1]
[1] CORIA, CNRS UMR6614, Normandie Université, UNIROUEN, INSA of Rouen, France
[2] Univ. Grenoble Alpes, CNRS, LEGI UMR 5519, Grenoble, F-38041, France
[3] Institut Universitaire de France (IUF), 75000 Paris, France

NOMENCLATURE

AM	Additive manufacturing
(C)HX	(Compact) heat exchanger
ES	Effective slope
f	Fanning friction factor
H	Half height channel
Ku	Kurtosis
Pr	Prandtl number
Re	Reynolds number
Re_τ	Shear Reynolds number
S_a	Arithmetic average height
S_q	Root-mean-square height
S_h	Maximum distance between peaks and valleys
Sk	Skewness
$\bar{Z}$	Passive scalar

INTRODUCTION

In aeronautical engines, heat exchangers have a fundamental role especially in controlling the temperature of the liquid fuel and oil streams. The mass of heat exchangers is also critical to reduce the total weight of the engine. The design of compact and efficient heat exchangers (CHX) is therefore of paramount importance for the future aeronautical engines. Additive manufacturing (AM) offers the opportunity to explore new designs and boost the optimization of CHX. [1]. For instance, as shown by Saltzman *et al.* [2], they obtained an improvement around 10 percent compared to heat exchangers built with traditional manufacturing.

Nonetheless, surface roughness generated with AM can be substantially larger than with traditional manufacturing techniques. Surface state of metal

AM test samples analysed in several studies have indeed underlined this key point [2, 3, 4, 5, 6, 7]. Moreover the wall roughness is not isotropic in space and varies according to the main direction of printing [4, 5]. Some patterns called welding tracks can appear on the surface [3]. This typical roughness has a significant impact on the performances in terms of pressure drop and heat transfer capacity [2, 6, 7]. In addition, an important gap between performances obtained from simulations and/or empirical correlations and those measured a posteriori exists.

Many papers have been devoted to the study of turbulent flow over different roughness types and surfaces experimentally [8] as well as numerically [9, 10, 11]. The presence of surface roughness causes an overall thickening of the boundary layer in addition to the modification of the streamwise structures. Secondary flow motions can also be observed due to spanwise inhomogeneities on the surface and this induces a better flow mixing. In addition, the transition between laminar to turbulent regimes appears earlier than over smooth surfaces. Concerning the mean velocity profile, a downward shift compared to the log-law profile is observed [12, 13]. The latter is commonly called the roughness function (ΔU^+). Roughness has also an impact on the Nusselt number since the increase of surface exchange enhances heat transfer [14].

Despite a better understanding of the flow behavior over inhomogeneous rough surfaces, some attempts have been performed to get a universal correlation for evaluating the equivalent sand-grain roughness height k_s [15, 16, 7]. This parameter k_s can be expressed as a function of the statistical roughness parameters such as the arithmetic average height (S_a), the root-mean-square height (S_q), the skewness (Sk) and the kurtosis (Ku). The two latter correspond respectively to the third and the fourth moments of the height distribution of the surface. Studies have underlined the predominance of the effective slope (ES), defined as the average slope of the surface height along the streamwise direction, in predicting roughness effects [10].

$$S_a = \frac{1}{L_x L_y} \int_{L_x} \int_{L_y} \mid h(x,y) \mid \, dxdy \tag{1}$$

$$S_q = \sqrt{\frac{1}{L_x L_y} \int_{L_x} \int_{L_y} h(x,y)^2 \, dxdy} \tag{2}$$

$$Sk = \frac{1}{{S_q}^3 L_x L_y} \int_{L_x} \int_{L_y} h(x,y)^3 \, dxdy \tag{3}$$

$$Ku = \frac{1}{{S_q}^4 L_x L_y} \int_{L_x} \int_{L_y} h(x,y)^4 \, dxdy \tag{4}$$

$$ES = \frac{1}{L_x} \int_0^L \mid \frac{dh}{dx} \mid dx \tag{5}$$

where $h(x,y)$ is the surface height, the mean plane is supposed to be at $h = 0$, L_x and L_y are respectively the streamwise and spanwise lengths.

A well-known threshold equal to $ES \approx 0.35$ delimits two regimes: i) the sparse or waviness regime below this limit and ii) the roughness or dense one [17]. Nevertheless, such universal correlation that would cover the two regimes has not been found up to now. Furthermore, few articles propose numerical simulation of AM surfaces.

In the aim of building new rough-wall models dedicated to AM surfaces, the creation of a roughness-resolved Large-Eddy Simulation (RRLES) database of representative channel flows emerges as a worthwhile process. The present paper describes a methodology to perform parametric RRLES from a limited set of surface parameters to control the surface height distribution and the streamwise and spanwise spatial auto-correlation functions. The first section of the article describes the numerical setup, configurations and the used methodology for performing RRLES. The post-processing and obtained results are presented and discussed in the second section.

NUMERICAL SETUP

In this section, chosen configurations and methodology are addressed. In order to ensure periodic channels, recycling conditions are applied on velocity and temperature. This process is particularly exposed here.

Configurations and Meshes

First of all, rough surface (RSG) and body-fitted unstructured mesh (RRMG) generators have been developed [18]. The former creates triangulated surfaces stored in the STL format that are used by the latter to compute level set functions. The level set functions are then employed to refine an existing 3D unstructured mesh and to create a conforming body-fitted mesh with controlled cell size, quality and size gradation. The resulting meshes are suitable for performing RRLES with higher-order finite-volume schemes. The RRMG has been developed within the YALES2 code. YALES2 is an unstructured low-Mach number code developed at CORIA for the Direct Numerical Simulations and Large-Eddy Simulations in complex geometries [19]. It heavily relies on the parallel volume and surface mesh adaptation.

The RSG/RRMG are utilized to generate rough planar channels but may also be applied to more complex shapes such as cylindrical tubes or plate/fin configurations. RRLES are conducted for periodic channels of size $8H$ x $3H$ x $2H$ in the streamwise (x), spanwise (y) and crosswise (h) directions with H the half height of the channel which is equal to 1.0 mm. This domain size was confirmed to be sufficient to have a negligible impact of the periodic recycling on the wall friction [20]. In addition, the half height was selected in order to be close to hydraulic diameters and channel heights encountered for some AM experiments as the L-2x-In case in Stimpson *et al.* [14].

Concerning the chosen configurations, three different cases representing two printing directions plus a streamwise and spanwise isotropic case have been selected for analysis. A smooth channel is also considered as a reference. Roughness parameters which are targeted in this article are the root-mean-square

height (S_q), the height distribution skewness (Sk) and kurtosis (Ku) and the effective slope (ES). While the surface height distributions are the same in the three cases, the effective slope is different due to the different space auto-correlation functions.

In addition of printing direction, the idea is to generate surfaces which mimic roughness height distribution encountered in AM. An overall range of roughness parameters values can be found in the literature even though there are differences between upward- and downward-facing surfaces [2, 3, 4, 5, 6, 7]. For this purpose, values of the latter for S_q, Sk and Ku are set respectively to 20 μm, around 0.2 and 4.0. Final values are exposed in Tab. 1 and probability density functions of height are plotted in Fig. 2 for the three geometries.

	ES	S_a (μm)	S_q (μm)	S_h (μm)	Sk	Ku
Front	0.29	15.6	20.0	187	0.21	3.92
Parallel	0.06	15.6	20.0	181	0.21	4.01
Isotropic	0.24	15.6	20.0	216	0.21	3.90

Table 1: ROUGHNESS PARAMETERS OF CHOSEN GEOMETRIES

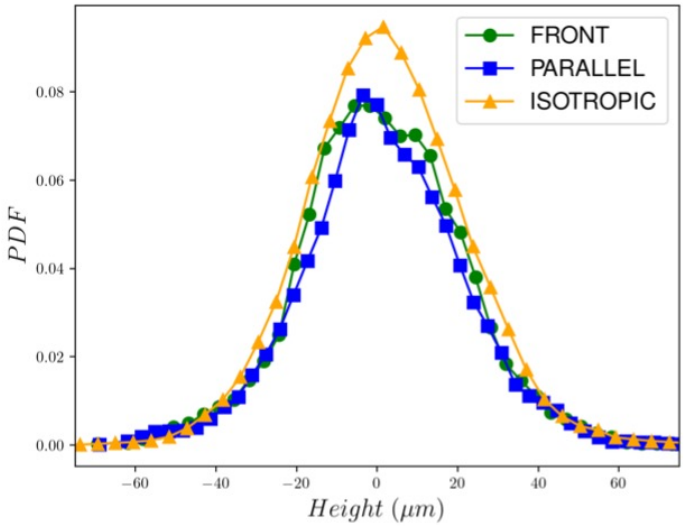

Figure 2: PROBABILITY DENSITY FUNCTION OF HEIGHT FOR THE THREE CASES

With the RRMG, conforming body-fitted meshes are obtained from these geometries. A balance on the element count has to be reached in order to resolve sufficiently the flow while minimizing the cost. In addition, the meshing process has to keep the topology intact. The mesh generation process starts from a cartesian grid which is tessellated and adapted numerous times.

The initial numbers of elements in each direction (N_x, N_y, N_h) for the cartesian grid are fixed in order to initially get isotropic cells of 20 μm. The cell size gradient is equal to 0.1 and the cell size on the rough surface is set to $\Delta y_w = 7$ μm. The final number of mesh elements for RRLES is about 130 million cells.

All characteristics and performances of meshing process are summarized in tables Tab. 2 and Tab. 3. The mesh for the smooth case is a stretched cartesian grid with the dimensionless wall grid spacing of $\Delta_x^+ = 13.7, \Delta_y^+ = 5.5, \Delta_h^+ = [0.5, 7.3]$ in accordance with operating conditions.

For each configuration, the mesh size is fixed for all the tested Reynolds numbers. The mesh resolution for the present study is discussed in the appendix. It must be noted that the dimensionless roughness $S_a/\Delta y_w$ is only larger than two, which may seem insufficient for the wall resolution. However, with body-fitted grids, this latter has to be sufficient for capturing the wall roughness (curvature and position as illustrated in Fig. 3) and the wall-normal velocity gradient.

Parameters	**Values**
L_x, L_y, L_z (mm)	$8.0; 3.0; 2.0$
Initial N_x, N_y, N_z	400 ; 150 ; 100
Cell size on STL	7 μm
Max cell size gradient	0.1

Table 2: MESHING CHARACTERISTICS

	ES	Cells	CPUs	CPU hours	RAM /CPU
Front	0.29	130.1M	1024	4096h	294Mb
Parallel	0.06	129.7M	1024	4198h	292Mb
Isotropic	0.24	122.9M	1024	5307h	279Mb

Table 3: MESHING PERFORMANCES

Statistics and Performances

For collecting statistics, each RRLES is split into two steps. The initialization step is performed during a given transient time and then statistics are accumulated. For each step, the durations are summarized in Tab. 4. For the second step, the dimensionless time t^+ defined by $t^+ = \frac{tu_\tau}{H}$ is around 20 in average. Interestingly, due to inhomogeneities of the surface, the time to establish a fully-developed turbulent channel flow is reduced compared to smooth cases.

RRLES CPU costs are presented in Tab. 5. For clarity, the CPU hours are averaged over all Reynolds numbers cases for each configuration.

Re	Init run (ms)	FTT Init	Stats run (ms)	FTT Stats
5000	0.7	8.8	4.0	50.6
8000	0.5	10.7	2.4	51.2
17 000	0.3	12.7	1.2	51.0
25 000	0.02	12.7	0.8	50.7

Table 4: TIME ACCUMULATION FOR STATISTICS (FTT: FLOW-THROUGH TIME)

	ES	Cells	CPUs	CPU hours
Front	0.29	130.1M	560	32 800h
Parallel	0.06	129.7M	560	18 500h
Isotropic	0.24	122.9M	560	32 500h

Table 5: RRLES PERFORMANCES

Numerics and Models

Working hypotheses

In each case, incompressible flow simulations are performed. The chosen target bulk Reynolds number range is the fully developed turbulent flow. This is why, RRLES are performed at $Re = 5\ 000$, $Re = 8\ 000$, $Re = 17\ 000$ and $Re = 25\ 000$. The fluid kinematic viscosity is set to $\nu = 1.517\ 10^{-5}\ m^2/s$ and the maximal CFL number used is equal to 0.8. The WALE subgrid scale model is retained as it is widely used for LES of boundary layer flows [21]. A fourth-order central finite-volume scheme is used and the four-step fourth-order scheme TFV4A is applied for velocity and scalar transport prediction [22].

Methodology, boundary conditions

The automatic generation of fully periodic channels is very challenging and ensuring periodic meshes is complex for unstructured grid. The periodicity is though necessary to reach statistical convergence of the flow. Instead of imposing strict periodic boundary conditions in the streamwise and spanwise directions, a Lagrangian recycling method has been developed. This method does not require to add a body force as source term in Navier-Stokes momentum equation to compensate the wall friction. This approach can also be used as a precursor in spatially developing boundary layers by increasing L_{out}. The idea behind this recycling method is simply to use a time-varying inlet boundary condition with a velocity coming from a distant plane in the channel. This 3-step recycling process is based on passive Lagrangian particles as illustrated in Fig. 4. A flow rate is imposed at the inlet and for optimizing performances, the recycling is done every N time steps, $N > 1$. A linear interpolation in time is performed between two recycled planes. No rescaling is applied on velocity

profile as such profile is unknown a priori. Thus, contrary to what is proposed in Xiao *et al.* for instance, no target or corrections on velocity field are applied as input of this method. In this article, we select $N = 20$ as it gives the better compromise between performances and velocity interpolation errors.

The complete process is described here:

1. Lagrangian particles are created at the inlet of the grid (blue spheres in Fig. 4) and are translated to the recycling plane.
2. The target field at the recycling plane, for instance velocity, is interpolated for translated particles (red spheres in Fig. 4)
3. This is the relocation step: particles are transferred at the inlet and the field at this location is updated.

The computational domain is then defined with a recycling zone and a buffer area to avoid any influence of the outlet boundary treatment onto the recycled velocity. Thus the location of the recycling plane is primordial and should be set at a given distance from the outlet within the domain. For two parallel planes, this distance was found to be at least equal to the length between both planes and in our cases, the latter corresponds to $2H$. Indeed, perturbations of the velocity field due to the outlet boundary condition may be recycled and injected at the inlet if L_{out} is below this threshold.

In order to decrease interpolation margin errors between the inlet and the recycling plane, both locations should be the equivalent at the wall. The generated rough surface and conformal mesh both respect this periodicity condition only in terms of wall topology. A no-slip wall boundary condition is applied on rough planes and the other sides in the spanwise direction are considered as slip walls. This methodology is also applied in the smooth configuration. Validation of the numerical methods may be found in the appendix.

Finally, from STL generation to post-processing, all calculation steps are integrated into a workflow tool. This allows to manage automatically series of runs on a distant super-computer.

SIMULATION ANALYSIS

This section details the different tools used for the subsequent analysis of the RRLES.

Non-dimensional velocity and temperature

For scaling velocity and temperature profiles, a calculated effective distance introduced by Kuwata & Kawaguchi [20] is used. Indeed, due to irregularities of the surface height, this kind of distance is not straightforward to determine as in a smooth-wall case. The effective distance is defined in Eq. 6 with h_w the minimal height of the surface. The variable φ corresponds to the x-y plane porosity which is the ratio between the x-y plane surface occupied by the fluid and the total x-y plane area.

$$h_e = \int_{h_w}^{h} \varphi \, dh \tag{6}$$

Computation of the friction velocity u_τ (Eq. 7) is based on the difference between average pressure at the inlet and at the recycling plane as exposed in Fig.6. The shear Reynolds number is then calculated as $Re_\tau = \frac{u_\tau H}{\nu}$. and the quantity h_e^+ is defined as $h_e^+ = \frac{h_e u_\tau}{\nu}$.

$$u_\tau = \sqrt{H \frac{\langle p_i \rangle - \langle p_r \rangle}{\rho L}} \tag{7}$$

Concerning the friction factor, the Fanning definition $f = 2\left(\frac{u_\tau}{U_b}\right)^2$ is used with U_b the bulk velocity. All these quantities are monitored at each iteration in the LES simulation.

For the analysis of heat transfer, a passive filtered scalar $\bar{Z}$ is used. This latter can be defined as $\bar{Z} = \frac{\bar{T} - T_p}{T_\infty - T_p}$ with T_p the temperature imposed at a wall and T_∞ the bulk temperature. This scalar is considered passive and this hypothesis is valid if the temperature difference has no significant impact on the density, which is assumed here. This is why, the temperature can be replaced by this dimensionless scalar. The equation for this scalar is the following:

$$\frac{\partial \bar{Z}}{\partial t} + \nabla \cdot (\bar{u}\bar{Z}) = \nabla \cdot (D_z \nabla \bar{Z}) \tag{8}$$

Thus, $\bar{Z} = 1$ is imposed at the upper wall and $\bar{Z} = 0$ everywhere including the bottom wall. The laminar Prandtl number Pr of this scalar is set to $Pr = 0.71$ and the turbulent Prandtl number is equal to unity. The diffusivity D_z includes the molecular and turbulent diffusivities.

Budget equations

In the present RRLES, different turbulence budget equations have been computed, dumped and stored. This is the case for the mean kinetic equation (Eq. 9). Quantities denoted with the bracket $\langle\rangle$ symbol are time-averaged and u' corresponds to the fluctuating component of velocity within the Reynolds decomposition. The quantity ν_t refers to the turbulent viscosity which is modeled through the WALE model.

Mean Kinetic Equation (MKE)

$$
\begin{aligned}
&\underbrace{\frac{1}{2}\frac{\partial\langle u_i\rangle\langle u_i\rangle\langle u_j\rangle}{\partial x_j}}_{1}+\underbrace{\frac{\partial\langle u_j\rangle\langle p\rangle}{\partial x_j}}_{2}\\
&+\underbrace{\frac{\partial\left\langle u_i\right\rangle\left\langle\tau_{ij}^{SGS}\right\rangle}{\partial x_j}}_{3}-\underbrace{2\frac{\partial\left\langle u_i\right\rangle\left\langle\nu S_{ij}\right\rangle}{\partial x_j}}_{8}+\underbrace{\frac{\partial\left\langle u_i\right\rangle\left\langle u_i'u_j'\right\rangle}{\partial x_j}}_{4}\\
&=\underbrace{\left\langle S_{ij}\right\rangle\left\langle\tau_{ij}^{SGS}\right\rangle}_{5}+\underbrace{\left\langle S_{ij}\right\rangle\left\langle u_i'u_j'\right\rangle}_{6}-\underbrace{2\left\langle S_{ij}\right\rangle\left\langle\nu S_{ij}\right\rangle}_{7}
\end{aligned}
\tag{9}
$$

with $\tau_{ij}^{SGS}=-2\nu_t S_{ij}$ and $S_{ij}=\frac{1}{2}\left(\frac{\partial u_i}{\partial x_j}+\frac{\partial u_j}{\partial x_i}\right)$.

RESULTS AND DISCUSSION

In this section, the wall-unit velocity and temperature profiles as well as the momentum and kinetic energy balance equations described in the previous section are analyzed. This analysis should provide a better understanding of the impact of the wall roughness on the flow and especially the effective slope parameter.

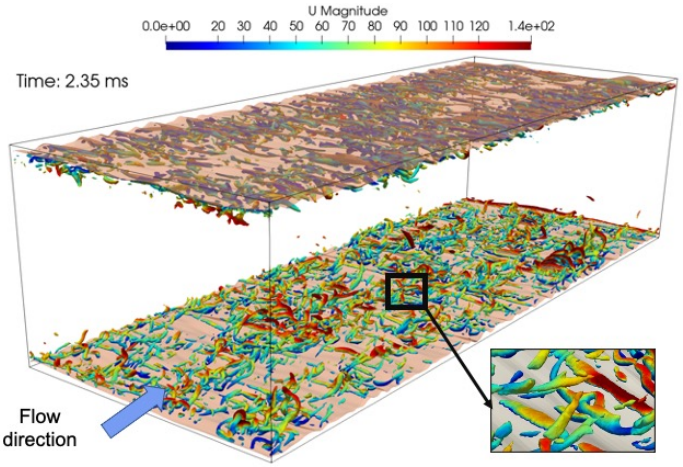

A) FRONT CASE $(ES = 0.29)$

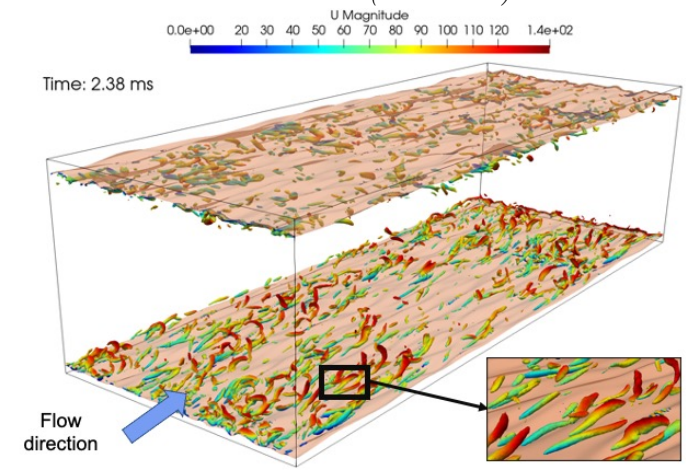

B) PARALLEL CASE $(ES = 0.06)$

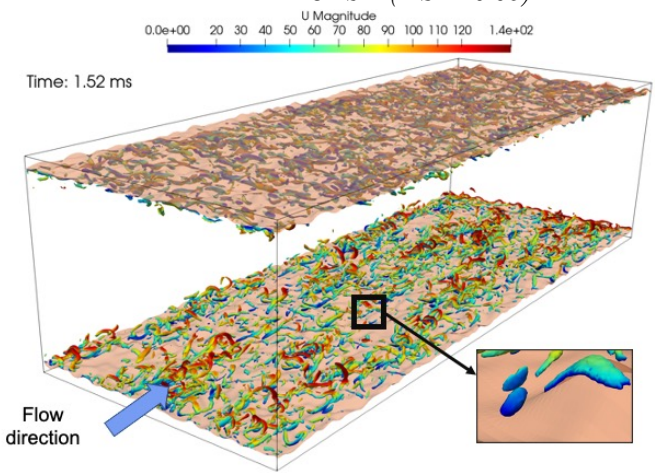

C) ISOTROPIC CASE $(ES = 0.24)$

Figure 7: Q-CRITERION ISO-CONTOUR COLORIZED BY VELOCITY AT RE = 8 000

Impact on Turbulence

A first qualitative analysis can be done by visualizing the vortices which are generated over the rough surface. The same Q-criterion iso-contours are plotted for the three different cases in Fig. 7 at a Reynolds number of 8 000. At a first glance, it is clearly noticed that the parallel case promotes elongated vortices in the flow direction while the two other cases also feature small vortices trapped between valleys. These trapped vortices are more coherent in the front case due to the orthogonal wavy pattern of the wall. Even if the roughness height distribution is the same, important differences are visually perceptible.

Mean streamwise velocity profiles are plotted in Fig. 8 for the three cases at Reynolds numbers of 8 000 and 17 000 as well as the smooth wall configuration. The impact of ES is clearly visible as the velocity profile is shifted downward with increasing ES. Differences are also noticeable between isotropic and anisotropic surfaces. Indeed, if the ES in isotropic case is lower than the front configuration, the mean velocity near the wall has a steeper increase for the isotropic case. These results indicate that the orientation of the wall roughness has a non-linear impact on the mean velocity in the channel. Moreover, increasing the Reynolds number tends to shift downward the profile in the log-law region as expected.

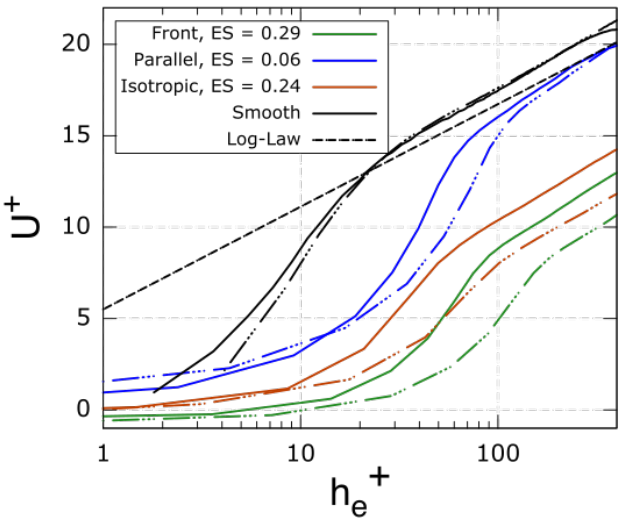

Figure 8: VELOCITY PROFILES (RE = 8 000 CONTINUOUS LINE, RE = 17 000 DASHED LINE)

Concerning, the fluctuating velocity, streamwise and spanwise components are plotted for Reynolds numbers Re = 8 000 Re = 17 000 in Fig. 9 and 10, respectively. For the streamwise fluctuating velocity u_{rms}, and considering the two anisotropic cases, the ES has an impact on the maximum value and this latter is shifted to the flow stream when changing the roughness direction. This

peak is also less pronounced for higher ES value. As for the mean velocity, the isotropic case has a slightly different behavior and while its ES value is in between the two anisotropic cases, the u_{rms} profile is not in between the two of the anisotropic cases confirming the non-linear behavior of the rough wall with ES.

For spanwise velocity fluctuations, the maximum of the profile is less affected by the geometry but its location follows the same trend as the streamwise fluctuations. Increasing the Reynolds number to 17 000 tends to shift the peaks to the channel center, to reduce the sharpness of the peaks for both velocity fluctuations and to slightly increase the maximum value of peaks for spanwise fluctuations.

The reduction of the anisotropy of the velocity fluctuations observed in each case in comparison with the smooth configuration is consistent with previous studies [23, 9]. It has been shown that this is caused by the redistribution of the mean roughness wake kinetic energy into turbulence, generating additional normal and spanwise stresses[24]. The streamwise turbulence is also mainly converted into wake energy as the streaks are destroyed by the roughness elements. Increasing the Reynolds number contributes to intensify this phenomenon.

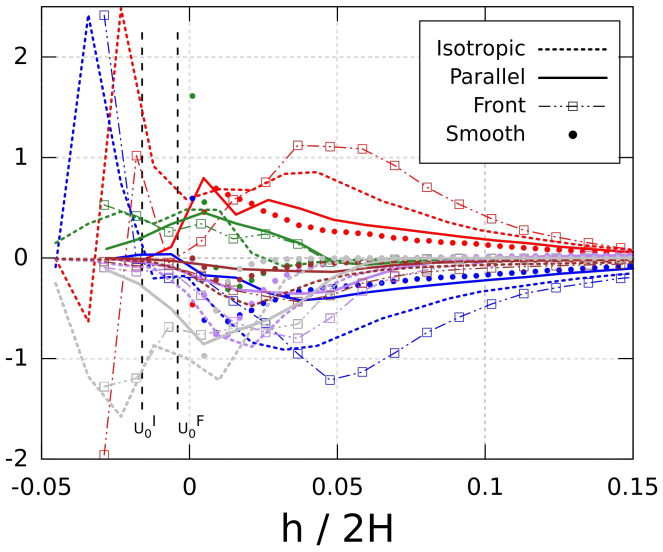

Figure 11: MEAN KINETIC BUDGET TERMS FOR $RE = 8000$ NORMALIZED BY u_τ^4/ν FROM SMOOTH CASE. 1: ——, 2: ——, 4: ——, 6: ——, -7: ——, 8: ——. U_0^I, U_0^F REFER TO MEAN VELOCITY CROSS-ZERO SCALES FOR ISOTROPIC AND FRONT CASES.

The presence of the wake is slightly visible on the mean velocity profiles when they become negative in the near-wall region for the isotropic and front cases. Mean kinetic energy balance plotted in Fig. 11 shows that this region is dominated by the work of the pressure drag against the flow direction. Those

observations are no more valid for the parallel case since the surface topology does not create significant re-circulation zones, letting the viscous drag to be dominant. Thus, the decreasing of the turbulence anisotropy and the pressure loss are less pronounced for this case.

For each Reynolds number and all roughness types, the roughness velocity function ΔU^+ is studied. The latter is evaluated at $h_e^+ = 100$ and compared to the boundary-layer log law. Results are summarized in Tab. 6. The first remark is that ΔU^+ is amplified with higher Reynolds number. Values are mainly higher in the front case except at $Re = 25\ 000$ where the isotropic case has a larger value. These results point out that the additive manufacturing direction has a strong impact on the mean velocity profile although roughness height distributions are the same.

ΔU^+	Re 5 000	Re 8 000	Re 17 000	Re 25 000
Front	5.90	7.84	11.1	13.9
Parallel	0.41	0.69	1.34	2.89
Isotropic	3.10	5.48	10.2	15.0

Table 6: ROUGHNESS FUNCTION VALUES EVOLUTION

Concerning the effect of the effective slope on pressure loss, the friction factor is investigated. The Colebrook correlation [25] (Eq. 10) is taken as a reference in order to compare friction factor values obtained in the present RRLES database to the Moody diagram. The definition used in this correlation is Darcy's one and the relationship between Darcy and Fanning friction factors is $f_{Darcy} = 4f$. Therefore, in Fig. 12, friction factors from the Colebrook equation are divided by a factor of 4 for getting comparative results. Two relative roughness S_a/D_h values ($S_a/D_h = 10^{-2}$ and $S_a/D_h = 5.10^{-3}$) for Colebrook formula are plotted as the relative roughness of the present cases is intermediate: $S_a/D_h = 7.8\ 10^{-3}$.

$$\frac{1}{\sqrt{f_{Darcy}}} = -2\log\left(\frac{S_a}{3.7D_h} + \frac{2.51}{Re\sqrt{f_{Darcy}}}\right) \tag{10}$$

As expected, for each Reynolds number, friction factor is higher with increasing ES. For the front and isotropic cases, values are above the Colebrook correlation ones and tend to slightly increase with the Reynolds number. However, the trend for parallel case is reversed: the curve is below Colebrook expectations and decreases. There is a clear distinction in the friction factor behavior when varying the printing direction. Therefore this correlation is inadequate for describing the tendency and evaluating a priori the friction factor. It also highlights again the need for better correlations for this type of roughness.

Impact on Temperature

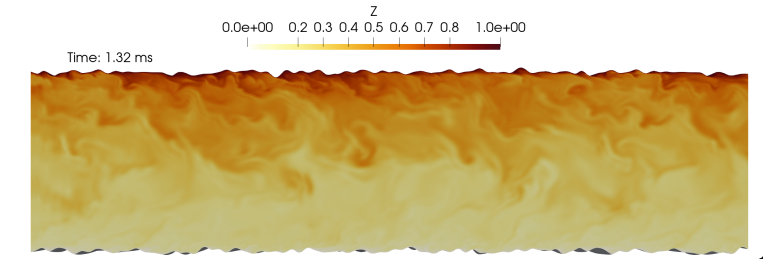

A) FRONT CASE ($ES = 0.29$)

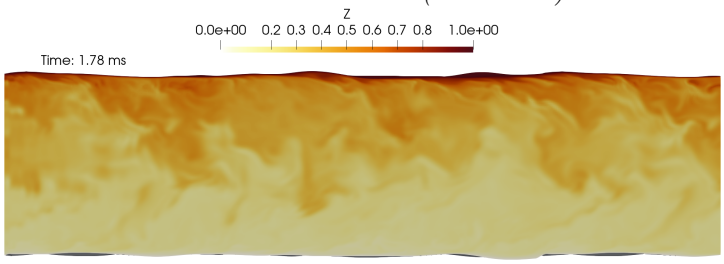

B) PARALLEL CASE ($ES = 0.06$)

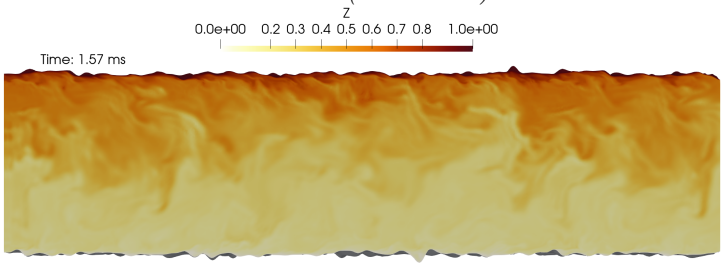

C) ISOTROPIC CASE ($ES = 0.24$)

Figure 13: INSTANTANEOUS TEMPERATURE FIELD AT $RE = 8\ 000$

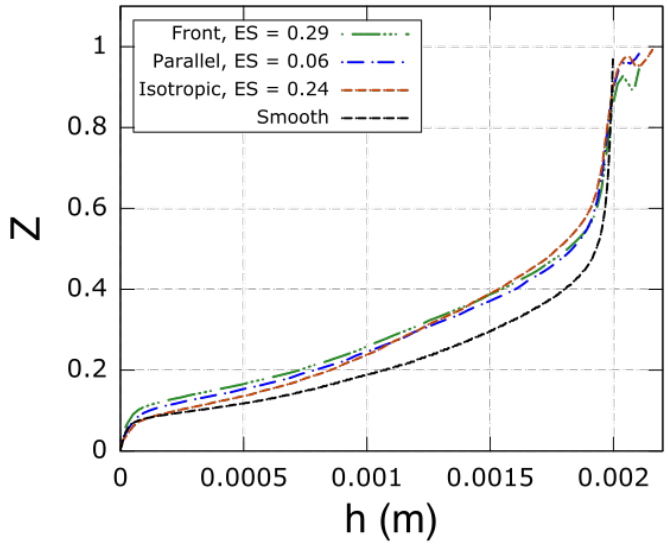

A) $RE = 8\ 000$

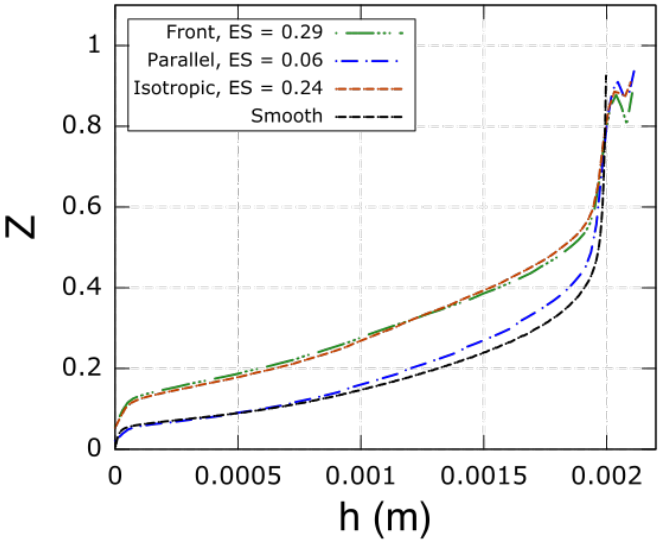

B) $RE = 17\ 000$

Figure 14: DIMENSIONLESS TEMPERATURE PROFILES

The roughness influence on heat transfer is also studied with this RRLES database. Indeed, modifications to the turbulent boundary layer induced by the roughness inhomogeneities can modify the temperature boundary layer and potentially the mean temperature field. As explained above, a passive scalar $\bar{Z}$ is transported and averaged (Eq. 8). Instantaneous $\bar{Z}$ field for the three rough cases are illustrated in Fig. 13. This figure shows that the temperature

fluctuations observed close to the wall have wave lengths similar to those of the wall roughness. This is particularly visible in the front and isotropic cases. In the parallel case, the chosen cut cannot represent the wall roughness as the roughness features are aligned with the cut plane. As a result, less short wave lengths are visible in this cut close to the wall.

In order to quantify if temperature transport by turbulence is enhanced by wall roughness or not, mean temperature profiles are plotted for two different Reynolds numbers in Fig. 14. At $Re = 8\ 000$ (Fig. 14a), the temperature transport in the boundary layer is enhanced by wall roughness as the mean temperature gradient increases towards a constant value in the whole channel height. The three rough cases have a slightly different behavior close to the wall. It seems that the isotropic case is the configuration that is the closest to the smooth case. For the two anisotropic cases, the presence of coherent structures in the roughness valleys seems to slightly increase the temperature wall gradient and thus the wall heat transfer.

For $Re = 17\,000$, the conclusions are different and more intuitive. Indeed, the parallel roughness and smooth cases have almost the same temperature profiles as it would be expected due to the alignment of the roughness elements with the flow. The front and isotropic cases have also the same temperature profile with a clear shift toward the constant gradient imaginary profile. In theses cases, the wall roughness promotes temperature transport by turbulence. For this higher Reynolds case, the dependence of the wall heat transfer with the effective slope is better recovered. Again, the different non-linear behaviors of the temperature with both the effective slope and the Reynolds number illustrate the challenge of finding a Nusselt number correlation for rough walls.

CONCLUSIONS

This paper presents roughness-resolved Large-Eddy Simulations that are representative of the flow obtained in additive-manufactured heat exchangers. The aim of these simulations is to provide a rich database that will ease the development and assessment of rough-wall models. The most challenging task in the building of this database is the generation of representative rough surfaces and conformal unstructured meshes. Three different configurations of parallel rough plane channels with the same roughness height distribution but different effective slopes have been chosen and modeled. The impact of the effective slope parameter, which is directly linked to the alignment of the wall roughness with the flow, has a strong impact on the flow topology, velocity and temperature profiles, as expected. In these cases, the existing empirical correlations find their limits and new correlations are needed.

acknowledgment

The STREAM project has received funding from the Clean Sky 2 Joint Undertaking (JU) under grant agreement No 865378. The JU receives support from the European Union's Horizon 2020 research and innovation program

and the Clean Sky 2 JU members other than the Union. This article reflects only the authors' view, the Joint Undertaking is not responsible for any use that may be made of the information it contains. This work was granted access to the HPC resources of CINES/TGCC/IDRIS under the allocation 2020-A0092B06880 and 2021-A0112B06880 made by GENCI and of CRIANN under the allocation 2012006.

Appendix: Numerical methods assessment

We validate our numerical methods by reproducing the classical $Re_\tau = 180$ pressure-gradient driven periodic-channel flow DNS test case from [26] (refered to as KMM hereafter). The geometry is $L_x = 4\pi H$, $L_y = 2\pi H$, $L_h = 2H$ with the same RRLES direction denomination and the dimensionless mesh resolution is $\Delta_x^+ = 8.6,\ \Delta_y^+ = 8,\ \Delta_h^+ = [0.38, 5.3]$. A first test (T1) is done with the periodic condition methodology and a second one (T2) uses the recycling boundary condition. For the latter, we set the recycling plane at a distance $2H$ above the outlet in the longitudinal direction and the input flow rate is chosen to impose the same bulk velocity measured in [26]. Results are summarized in Fig. .15. Good agreement between tests and references shows that our numerical schemes and recycling boundary condition are appropriate to perform infinite channel flow simulations.

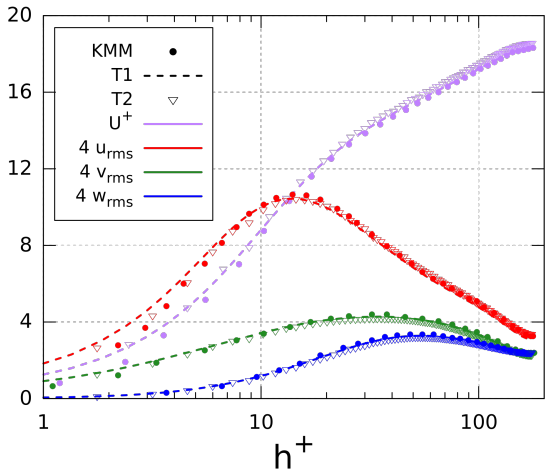

Figure .15: VELOCITY MEAN AND FLUCTUATION PROFILES IN THE CHANNEL FLOW TEST CASE.

We discuss now the RRLES mesh size used in this paper. Fig. .16 compares the results obtained from the $Re = 17\,000$ isotropic configuration with the mesh described in Tab. 2 (denoted M2) and those obtained with a coarser mesh (M1) whose cell size is 10 μm. It is seen that no significant differences may be observed between the two simulations, both on velocity first- and second-order

moments. This suggests that results will be probably weakly improved with a mesh finer than M2, for the analyzed moments. Thus, we consider that the dimensionless wall normal resolution y^+ obtained with the mesh M2 for this case is a satisfactory reference. Due to the surface alternating of peaks and valleys, making the wall normal mean velocity gradient to vary in space, it is more relevant to observe the statistical distribution of the wall resolution than its mean value alone to evaluate the mesh quality. Fig. .17 shows the probability density function of y^+ obtained for the considered Reynolds numbers. Obviously, the distributions for the two lowest Reynolds numbers are satisfactory. On the other hand, the distribution for $Re = 25\ 000$ is larger than our limit. Nevertheless, it is similar to the one obtained for $Re = 17\ 000$ with M1. According to previous results, we can consider that M2 is adequate for the simulations performed in this paper. Analysis for the front and parallel surfaces (not shown here) leads to the same conclusions.

References

[1] Carozza, A., 2017. "Heat exchangers in the aviation engineering". *Heat Exchangers - Advanced Features and Applications*.

[2] Saltzman, D., Bichnevicius, M., Lynch, S., Simpson, T., Reutzel, E., Dickman, C., and Martukanitz, R., 2018. "Design and evaluation of an additively manufactured aircraft heat exchanger". *Applied Thermal Engineering,* ***138***, pp. 254–263.

[3] Cabanettes, F., Joubert, A., Chardon, G., Dumas, V., Rech, J., Grosjean, C., and Dimkovski, Z., 2018. "Topography of as built surfaces generated in metal additive manufacturing: A multi scale analysis from form to roughness". *Precision Engineering,* ***2018.01.002***.

[4] Ventola, L., Robotti, F., Dialameh, M., Calignano, F., Manfredi, D., Chiavazzo, E., and Asinari, P., 2014. "Rough surfaces with enhanced heat transfer for electronics cooling by direct metal laser sintering". *Int. J. Heat Mass Transfer,* ***75***, pp. 58–74.

[5] Simonelli, M., Tse, Y., and Tuck, C., 2014. "Effect of the build orientation on the mechanical properties and fracture modes of slm ti–6al–4v". *Mater. Sci. Eng. A.,* ***616***, pp. 1–11.

[6] Snyder, J., Stimpson, C., and Thole, K., 2016. "Build direction effects on additively manufactured channels". *J. Turbomach.,* ***138***, pp. 1–8.

[7] Stimpson, C., Snyder, J., Thole, K., and Mongillo, D., 2017. "Scaling roughness effects on pressure loss and heat transfer of additively manufactured channels". *J. Turbomach.,* ***139***(2), p. 021003.

[8] Jiménez, J., 2004. "Turbulent flows over rough walls". *Annu. Rev. Fluid Mech.,* ***36***, pp. 173–196.

[9] Piomelli, U., 2019. "Recent advances in the numerical simulation of rough-wall boundary layers". *Phys. Chem. Earth.,* ***113***, pp. 63–72.

[10] Napoli, E., Armenio, V., and De Marchis, M., 2008. "The effect of the slope of irregularly distributed roughness elements on turbulent wall-bounded flow". *J. Fluid Mech.,* ***613***, pp. 385–394.

[11] Busse, A., Lutzner, M., and Sandham, N., 2015. "Direct numerical simulation of turbulent flow over a rough surface based on a surface scan". *Computers and Fluids,* ***116***, pp. 129–147.

[12] Clauser, F., 1954. "Turbulent boundary layers in adverse pressure gradients". *J. Aeronaut. Sci.,* ***21***, pp. 91–108.

[13] Hama, F., 1954. "Boundary layer characteristics for smooth and rough surfaces". *Trans. Soc. Nav. Arch. Mar. Engrs.,* ***62***, p. 333–358.

[14] Stimpson, C., Snyder, J., Thole, K., and Mongillo, D., 2016. "Roughness effects on flow and heat transfer for additively manufactured channels". *J. Turbomach.*

[15] Flack, K., and Schultz, M., 2010. "Review of hydraulic roughness scales in the fully rough regime". *J. Fluids Eng.,* ***132***, p. 041203.

[16] Forooghi, P., Stroh, A., Magagnato, F., Jakirlic, S., and Frohnapfel, B., 2017. "Toward a universal roughness correlation". *J. Fluids Eng.,* ***139***, p. 121201.

[17] MacDonald, M., Chan, L., Chung, D., Hutchins, N., and Ooi, A., 2016. "Turbulent flow over transitionally rough surfaces with varying roughness densities". *J. Fluid Dynamics,* ***804***, pp. 130–161.

[18] Meynet, S., Moureau, V., Lartigue, G., and Hadjadj, A., 2021. "Automatic surface and volume mesh generation for roughness-resolved les of additive-manufacturing heat exchangers". In ETMM13 Proceedings, ERCOFTAC. Paper number 105.

[19] Moureau, V., Domingo, P., and Vervisch, L., 2011. "Design of a massively parallel cfd code for complex geometries". *Comptes Rendus Mécanique,* ***339 (2-3)***, pp. 141–148.

[20] Kuwata, Y., and Kawaguchi, Y., 2019. "Direct numerical simulation of turbulence over systematically varied irregular rough surfaces". *J. Fluid Mech.,* ***862***, pp. 781–815.

[21] Nicoud, N., and Ducros, F., 1999. "Subgrid-scale stress modelling based on the square of the velocity gradient tensor". *Flow, Turbulence and Combustion*, pp. 183–200.

[22] Kraushaar, M., 2011. "Application of the compressible and low-Mach number approaches to Large-Eddy Simulation of turbulent flows in aero-engines". PhD Thesis, Institut National Polytechnique de Toulouse,, December.

[23] Shafi, H., and Antonia, R., 1995. "Anisotropy of the reynolds stresses in a turbulent boundary layer on a rough wall". *Exp. Fluid,* ***18***, pp. 213–215.

[24] Yuan, J., and Piomelli, U., 2014. "Roughness effects on the reynolds stress budgets in near-wall turbulence". *Journal of Fluid Mechanics,* ***760***, p. R1.

[25] Colebrook, C., 1939. "Turbulent flow in pipes, with particular reference to the transition region between the smooth and rough pipe laws". *Inst. Civil Eng.,* ***11***, pp. 133–156.

[26] Kim, J., Moin, P., and Moser, R., 1987. "Turbulence statistics in fully developed channel flow at low reynolds number". *Journal of Fluid Mechanics,* ***177***, p. 133–166.

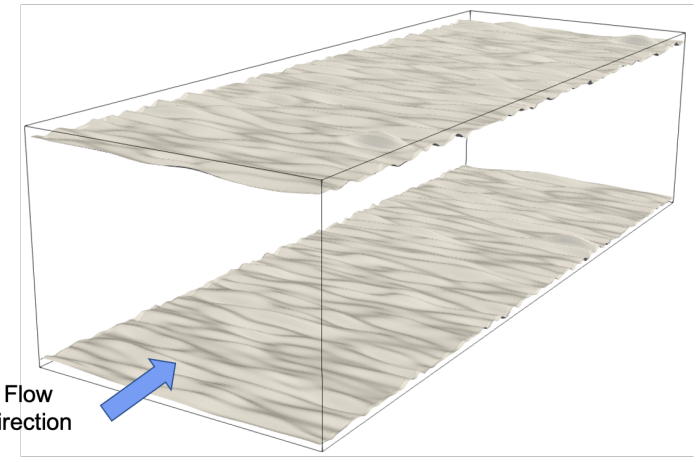

A) PERPENDICULAR PRINTING DIRECTION TO THE FLOW ($ES = 0.29$)

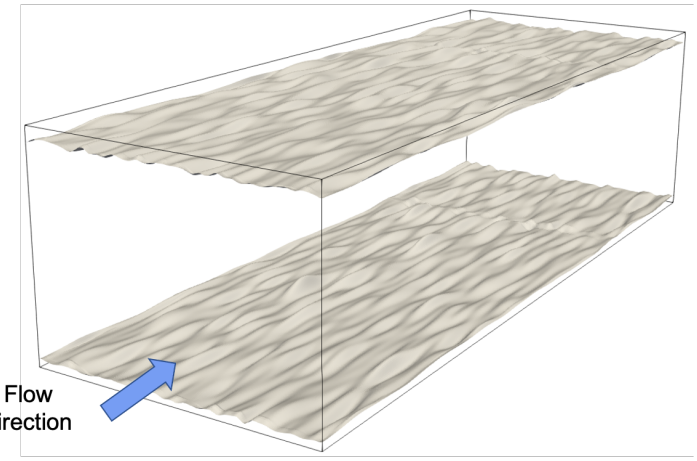

B) PARALLEL PRINTING DIRECTION TO THE FLOW ($ES = 0.06$)

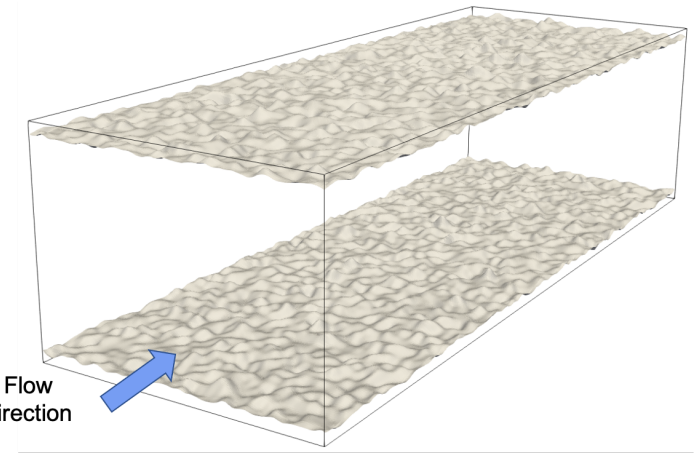

C) ISOTROPIC ROUGHNESS CASE ($ES = 0.24$)

Figure 1: GEOMETRY OF CONSIDERED CONFIGURATIONS

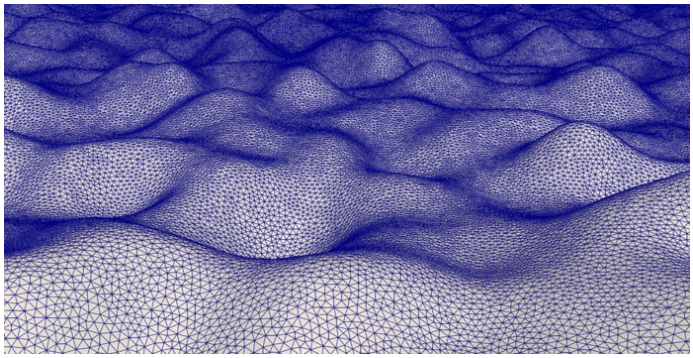

Figure 3: ZOOM-IN OF THE MESH ON THE UPPER SURFACE FOR ISOTROPIC CASE ($ES = 0.24$)

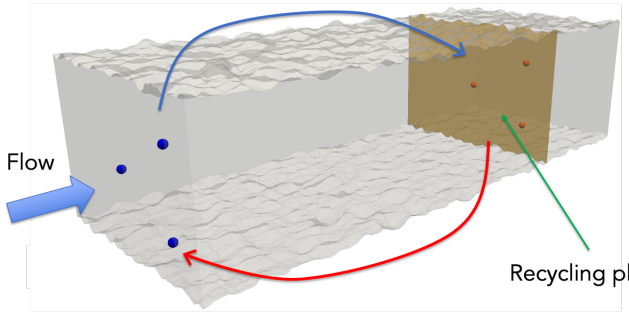

Figure 4: GENERAL PRINCIPLE OF THE DEVELOPED RECYCLING METHOD

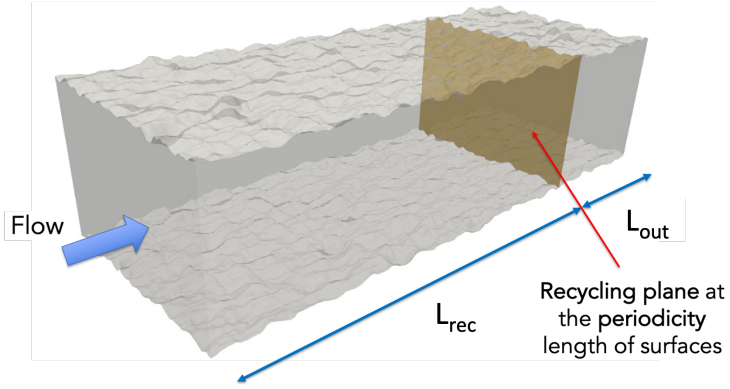

Figure 5: COMPUTATIONAL DOMAIN SPLIT INTO TWO AREAS: THE RECYCLING AND THE BUFFER ZONES

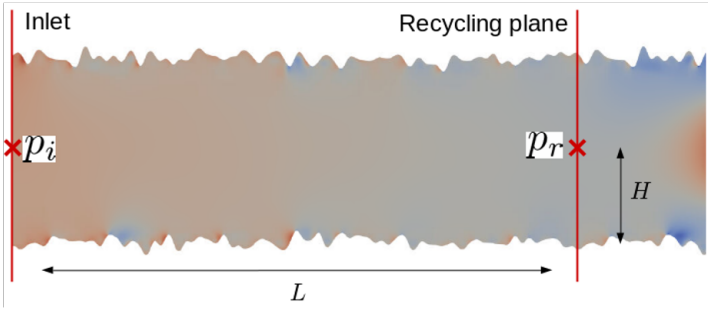

Figure 6: PRINCIPLE OF THE CALCULATION OF THE FRICTION VELOCITY

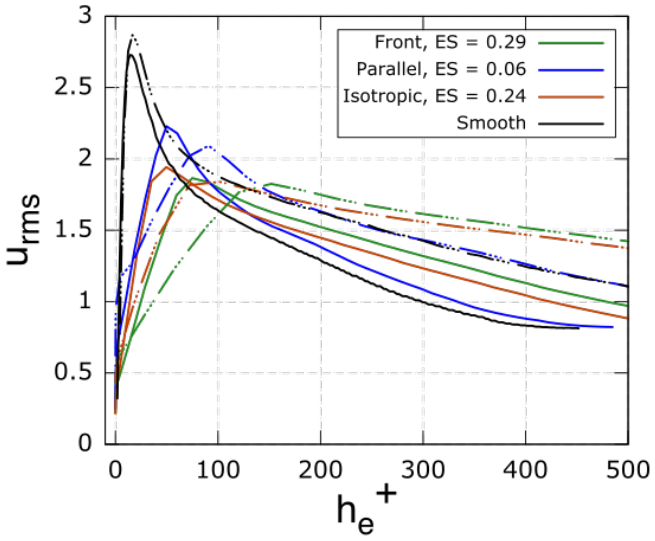

Figure 9: FLUCTUATION OF STREAMWISE VELOCITY (RE = 8 000 CONTINUOUS LINE, RE = 17 000 DASHED LINE)

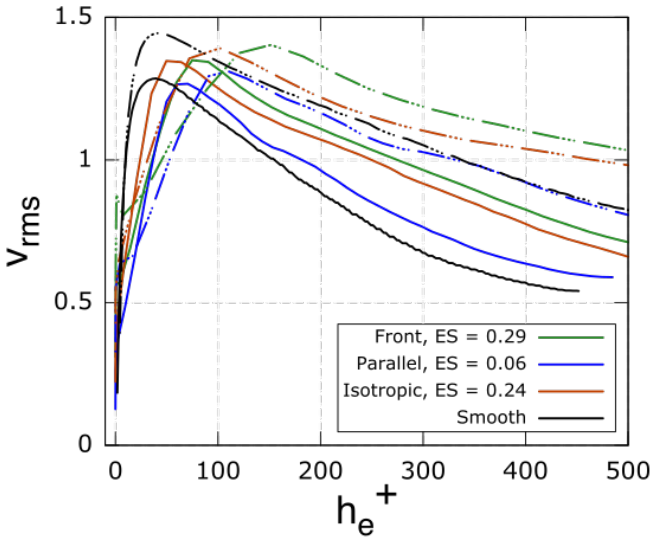

Figure 10: FLUCTUATION OF SPANWISE VELOCITY (RE = 8 000 CONTINUOUS LINE, RE = 17 000 DASHED LINE)

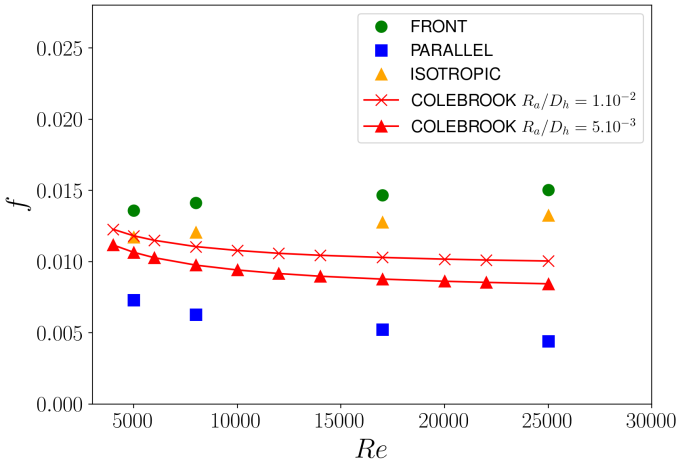

Figure 12: FRICTION FACTOR VALUES AT DIFFERENT REYNOLDS NUMBERS FOR EACH CASE

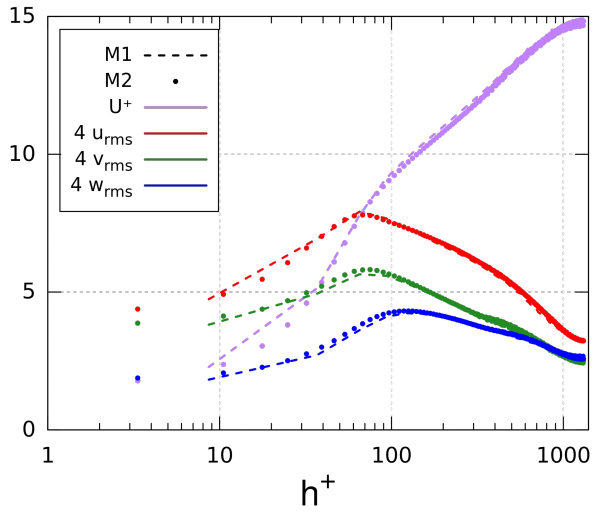

Figure .16: VELOCITY MEAN AND FLUCTUATION PROFILES FOR DIFFERENT MESHES FROM RRLES ISOTROPIC CASE, $RE = 17000$.

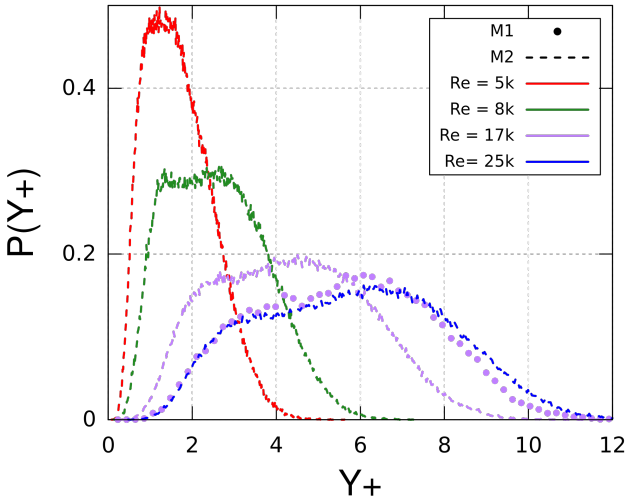

Figure .17: DIMENSIONLESS MEAN WALL RESOLUTION PDF FROM RRLES ISOTROPIC CASES.